Ab initio molecular dynamics study of the static, dynamic, and electronic properties of liquid Bi near melting using real-space pseudopotentials

J. Souto, M. M. G. Alemany, and L. J. Gallego
Departamento de Física de la Materia Condensada, Facultad de Física, Universidad de Santiago de Compostela, E-15706 Santiago de Compostela, Spain

L. E. González and D. J. González
Departamento de Física Teórica, Facultad de Ciencias, Universidad de Valladolid, E-47011 Valladolid, Spain
(Received 27 November 2009; revised manuscript received 8 February 2010; published 5 April 2010)

We perform a comprehensive study of the static, dynamic, and electronic properties of liquid Bi at $T=600$ K, $\rho=0.02876$ Å^{-3} by means of 124-atom *ab initio* molecular dynamics simulations based on PARSEC, a real-space implementation of pseudopotentials constructed within the density-functional theory. The predicted results are in good agreement with available experimental data, thus confirming the adequacy of this technique to achieve a reliable description of a nonsimple liquid metal such as liquid Bi, whose static structure has reminiscences of the rhombohedral structure of the crystal. The calculated intermediate scattering function $F(q,t)$ shows at low-q values a strong diffusive component which imposes a slow decay of this function. The dynamic structure factor $S(q,\omega)$ exhibits side peaks, indicative of collective density excitations, over a range of wave numbers up to $q\approx 1.4$ Å^{-1}. Moreover, our simulations suggest an important "positive dispersion effect" for the density fluctuations of around 20%. We have also investigated the relaxation mechanisms for the density fluctuations by analyzing the different contributions to the second-order memory function of $F(q,t)$. Our results suggest that the thermal relaxation is the slow decaying channel, whereas the viscoelastic relaxation is the fast decaying channel. This behavior is just the opposite of that found in some liquid metals and may be attributed to the semimetal character of Bi.

DOI: 10.1103/PhysRevB.81.134201 PACS number(s): 61.20.Ja, 61.20.Lc, 61.25.Mv, 71.15.Pd

I. INTRODUCTION

Molecular dynamics (MD) is a powerful simulation technique for the study of macroscopic and low-dimensional systems. MD results allow the assessment of the reliability of available theoretical approaches, also affording information on properties that would be very difficult or impossible to determine experimentally or simply have not been measured. In classical MD (CMD) simulations, the forces acting upon the atoms/ions are derived from interatomic potentials, the electronic degrees of freedom remaining hidden. By contrast, in *ab initio* MD (AIMD) simulations the forces are derived from electronic structure calculations which are performed as the MD trajectory is generated. In recent years, there has been a substantial increase in the application of AIMD methods based on the density-functional theory (DFT).[1,2] Given a collection of atoms/ions at specified positions, the DFT allows to determine their ground-state electronic energy as well as the forces on them. Consequently, in DFT-based AIMD simulations the atomic/ionic positions evolve according to classical mechanics while the electronic subsystem follows adiabatically.

This paper reports an extensive AIMD simulation study of the static, dynamic, and electronic properties of liquid bismuth (l-Bi) at a thermodynamic state close to the melting point ($T=544$ K). Solid Bi, Sn, and As are semimetals that crystallize in a rhombohedral structure, which may be regarded as a distorted simple cubic structure produced by an elongation along one of the [111] directions. This leads to a splitting of the first coordination shell into two subshells, each one containing three atoms. It has been reported[3] that l-As has a structure remarkably close to that of the crystal, whereas those of l-Bi and l-Sn still present similarities with their respective crystal structures, although less pronounced than in the case of l-As. Recently, it has been found that, at ambient pressure and $T\approx 1013$ K, l-Bi undergoes a temperature-driven liquid-liquid structural transformation, whose existence is supported by weak discontinuities in the temperature dependence of the coordination number, density, and heat capacity.[4]

The static structure factor $S(q)$ of l-Bi at temperatures near the melting point was determined by both neutron-scattering (NS) (Refs. 5 and 6) and x-ray (XR) (Ref. 7) measurements. $S(q)$ shows an asymmetric main peak along with a shoulder at its high-q side and the following oscillations are also clearly marked. The associated pair-distribution function $g(r)$ shows a rather symmetric first peak and its second maximum is shifted to relatively long distances compared with the behavior of simple liquid metals (SLMs). The first comprehensive inelastic NS (INS) measurements on l-Bi were performed by Dahlborg and Olsson[8,9] at $T=580$ K. They determined the dynamic structure factor $S(q,\omega)$ within the range $0.5\leq q\leq 7.2$ Å^{-1}, with the remarkable result of the absence, for $q\geq 0.6$ Å^{-1}, of collective density excitations, as evinced by side peaks in $S(q,\omega)$. Subsequently, these results were questioned by the INS measurements made by Shibata *et al.*[10] for l-Bi at 673 K within the range $0.6\leq q\leq 1.6$ Å^{-1}, as they found side peaks in $S(q,\omega)$ for a wider q range, namely, for $q\leq 1.2$ Å^{-1}. Sani *et al.*[11] have recently performed INS measurements for l-Bi at 580 K allowing to determine $S(q,\omega)$ in the range $0.15\leq q\leq 0.6$ Å^{-1}. The analysis of these data revealed the existence of collective

excitations along with a significant "positive dispersion effect" (i.e., an increase in the dispersion relation of the density fluctuations with respect to the hydrodynamic linear-dispersion relation) of ≈20%, which is of a magnitude similar to that found in other liquid metals.[12,13]

Several theoretical studies have been performed on the static, dynamic, and electronic properties of *l*-Bi using both semiempirical and more fundamental methods. Among the semiempirical studies, it is worth to mention those that basically resorted to the simple hard-sphere (HS) model. For instance, Umar and Young[14] used the HS model with a packing fraction calculated within the framework of a variational theory to obtain a reasonable estimate of $S(q)$ at melting, although it is known that the HS model can not account for shoulders. The HS model was also used by Ascarelli[15] to obtain reasonable predictions of the isothermal compressibility and the velocity of sound.

CMD simulations on *l*-Bi were made by Dzugutov and Dahlborg[16] using an interatomic pair potential derived by an iterative process which combines liquid state theories with the experimental data for $S(q)$. Dzugutov and Dahlborg used 16 384 particles and the smallest attainable q value was 0.078 Å^{-1}. The predicted $S(q,\omega)$ was in fair agreement with the experimental data at $T=580$ K,[8,9] although it showed side peaks up to $q=0.6$ Å^{-1} only. The associated adiabatic mode velocity had a hydrodynamic limit ($q\rightarrow 0$) value of 1520 m/s, somewhat smaller than the experimental result. CMD simulations were also performed by Hafner and Jank[17] in order to study some structural and electronic properties of *l*-Bi near melting. Hafner and Jank used an interatomic potential derived from a nonlocal pseudopotential with relativistic core functions. Interestingly, the interatomic potential used was purely repulsive at around the nearest-neighbor distance with a very small curvature. The main peak of their predicted pair-distribution function $g(r)$ was about 25% higher than the experimental value and $S(q)$ showed a peak instead of the expected high-q shoulder. The calculated electronic density of states (DOS) showed a valence band with a gap of ≈3 eV separating a *s* band at higher binding energy and a *p* band at the Fermi level. More recently, Bryk and Mryglod[18] have used CMD simulations to investigate the collective dynamics of *l*-Bi in terms of generalized collective modes. They found that, beyond the hydrodynamic region, the spectrum of the collective excitations had three branches of propagating excitations, namely, the generalized sound mode and two high-frequency kinetic branches. AIMD simulations on *l*-Bi were performed some time ago by de Wijs *et al.*[19,20] using a nonlocal ionic pseudopotential, but they were only concerned with the static and electronic properties. Moreover, the study was carried out with only 60 particles at a high temperature of 1000 K, and although the calculated $S(q)$ showed an overall good agreement with experimental data, the main peak was too pronounced and its position was slightly shifted to greater q values. To our knowledge, no AIMD study has hitherto been performed on the behavior *l*-Bi at thermodynamic states close to the melting point.

This paper reports the first comprehensive 124-atoms AIMD study of *l*-Bi at $T=600$ K using PARSEC, a DFT-based pseudopotential algorithm for real-space electronic calculations.[21] As it will be seen, the predicted results and available experimental data are in good agreement, which confirms the adequacy of this technique to achieve a reliable description of the behavior of a non-SLM such as *l*-Bi, including its dynamic properties. In particular, our results show the existence of collective density excitations over a range of wave numbers up to $q\approx 1.4$ Å^{-1}, which clarifies discrepancies between the results of different INS measurements.[8–11]

The layout of the paper is as follows. In Sec. II we briefly describe the formalism used in the present AIMD study, giving the technical details that are strictly necessary. In Sec. III we present and discuss our structural, dynamical, and electronic results, comparing them with available experimental data and with those of other simulation studies. Finally, in Sec. IV, we summarize our main conclusions.

II. COMPUTATIONAL METHOD

One of the most successful ways for obtaining the electronic structure of matter has been the use of computational approaches based on DFT. Among these approaches, real-space pseudopotential techniques have recently attracted special interest due to their computational advantages (see, e.g., Ref. 22). Pseudopotential theory allows one to focus on the chemically active valence electrons by replacing the strong all-electron atomic potential by a weak pseudopotential, which effectively reproduces the effects of the core electrons on the valence states. This approximation significantly reduces the number of eigenpairs to be handled, especially for heavier elements. Working in real space has a number of points in its favor. First, implementation of these approaches is simple: there is no "formal" basis, calculations being performed directly on a real-space grid that does not depend on ion positions; only one parameter, the spacing of the grid, needs to be refined to control convergence. Second, real-space methods are semilocal, which facilitates implementation on parallel computers. This makes such methods highly attractive for computation of the electronic structure of large, complex systems.

In this work, we adopted a real-space pseudopotential approach to study *l*-Bi. Specifically, we performed AIMD simulations using the PARSEC code.[21] In this method, the Kohn-Sham equations are solved self-consistently on a rectangular three-dimensional real-space grid within a supercell geometry.[23] The core electrons were represented by norm-conserving pseudopotentials generated for the reference configuration [Xe] $(4f^{14}\,5d^{10})6s^2 6p^3 6d^0 5f^0$ using the Troullier-Martins prescription[24] with a radial cutoff of 3.0 a.u. (1 a.u.=0.529 Å) for the *s*, *p*, *d*, and *f* channels. The potential was made separable by the procedure of Kleinman and Bylander[25] with the *p* potential chosen to be the local component. The partial-core correction for nonlinear exchange correlation was included. The local-density functional of Ceperley and Alder[26] was used as parameterized by Perdew and Zunger,[27] and the single Γ point was employed in sampling the Brillouin zone. A spacing of 0.64 a.u. was used for constructing the real-space grid. Calculations were performed for a thermodynamic state of *l*-Bi characterized by the number density $\rho=0.02876$ Å^{-3} and the temperature $T=600$ K (~50 K above the melting point). 124 atoms were

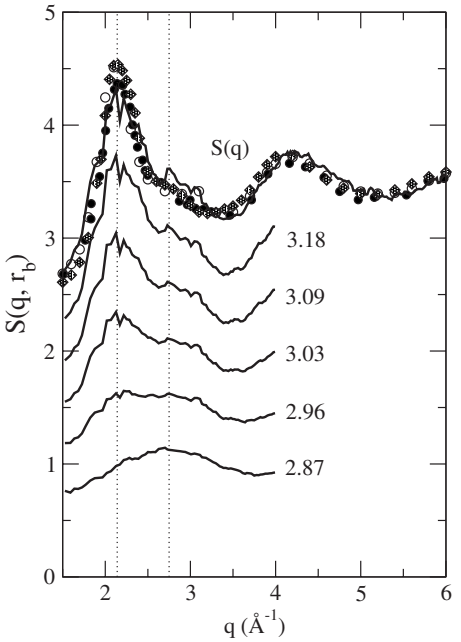

FIG. 1. Bonded-atom structure factor $S(q,r_b)$ obtained in our AIMD simulations of *l*-Bi at 600 K (solid lines); the numbers denote the values of r_b in angstrom, and the vertical dotted lines are drawn at the q values corresponding to the positions of the peak and the shoulder of $S(q)$. Open and full circles: experimental NS data for $S(q)$ from Dalhborg and Davidovič (Ref. 6) at 566 K and North *et al.* (Ref. 5) at 573 K, respectively. Diamonds: XR data at 573 K from Waseda (Ref. 7).

placed at random in a cubic supercell; the cell was coupled to a virtual heat bath via the Langevin equation of motion[28] and was heated to far above the target temperature in order to eradicate any memory of its initial configuration; the temperature was then set to 600 K, the system allowed to stabilize, and gradually decoupled from the virtual heat bath; and finally an AIMD simulation run was performed over 8000 time steps (40 ps of simulated time), ion dynamics being generated using the Beeman algorithm[29] with Hellmann-Feynman forces.[30] Only data from this latter simulation run were used in calculating the static, dynamic, and electronic properties reported below.

III. RESULTS AND DISCUSSION

A. Static properties

Figure 1 shows the static structure factor $S(q)$ obtained in our AIMD simulations of *l*-Bi at $T=600$ K. It has a main peak centered at $q_p \sim 2.15$ Å^{-1}, a shoulder and the subsequent oscillations are clearly marked. The computed $S(q)$ agrees very well with the experimental NS (Refs. 5 and 6) and XR (Ref. 7) data near melting.

The existence of the shoulder suggests a closer analysis of $S(q)$ in terms of the bonded-atoms structure factor $S(q,r_b)$, which is calculated as $S(q)$ but only considering those atoms with one or more neighbors within a distance r_b. The computed $S(q,r_b)$ is shown in Fig. 1 for several values of r_b. The main peak of $S(q,r_b)$ for $r_b \leq 2.87$ Å is at the position of the shoulder in the full $S(q)$, but around $r_b=2.96$ Å a second peak emerges at a smaller q value, which grows as r_b increases so as to become the main peak of $S(q)$. This behavior, which has also been found in AIMD simulations of *l*-Ga,[31,32] *l*-Si,[32] and *l*-Sn,[33] suggests that the shoulder in $S(q)$ is closely related to the existence of atoms separated by less than some critical distance, which for *l*-Bi is ≈2.87 Å. In those AIMD studies, it was found that at such separation the electron density along the line joining the atoms displays a charge accumulation resembling a covalent-bonding charge, which was interpreted as a signature of a short-lived diatomic molecular unit. We have also performed AIMD calculations for the Bi_2 dimer using PARSEC to obtain a bond length of ≈2.60 Å. Calculations performed by Gao *et al.*[34] using the VASP code gave a similar value of ≈2.66 Å.

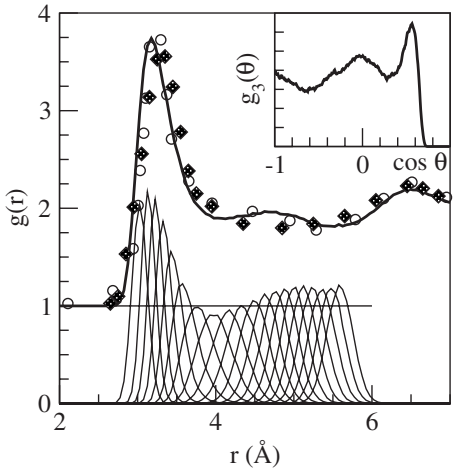

FIG. 2. Pair-distribution function (displaced by one unit) $g(r)$ obtained in our simulations of *l*-Bi at 600 K (thick line). Open circles: XR data at 566 K from Dahlborg and Davidovič (Ref. 6). Gray diamonds: XR data at 573 K from Waseda (Ref. 7). The thin lines represent the computed partial RDF $G_i(r)$, $i=1,2,\ldots,20$. The inset shows our predicted bond-angle distribution function.

Closely related to $S(q)$ is the pair-distribution function $g(r)$, which provides additional insight into the short-range order in the liquid. The experimental $g(r)$ has a symmetric main peak located at $r_p \approx 3.25$ Å followed by a shoulder and the minimum is located at ≈5.5 Å while the second maximum is at ≈6.5 Å.[6,7] Figure 2 shows a fair agreement between our computed $g(r)$, which has the main peak at ≈3.30 Å, and the experimental data. To evaluate the average number of nearest neighbors (also known as the coordination number, N_c) a number of ways have been proposed.[35] Integration of the radial distribution function (RDF) $G(r)=4\pi r^2 \rho g(r)$ up to the position of its first minimum, $R_{\min}=3.95$ Å, leads to the value $N_c \sim 7.4$. Another possibility would be to identify $R_{\min}$ with the position of the first minimum of $g(r)$, i.e., $R_{\min}=4.1$ Å, which gives $N_c \sim 8.0$.

We have also analyzed the distribution of nearest neighbors, as predicted by our AIMD simulations. To this end, we have resorted to McGreevy's ideas,[35] where the basic magnitude is the partial RDF $G_i(r)$ $(i=1,2\ldots)$. $G_i(r)$ is related to the probability of finding the ith neighbor of a particle at a distance r, so that $G(r)=\Sigma_i G_i(r)$. The borderline between two coordination shells is suggested to be located at that

$G_i(r)$ whose peak height is a minimum and the average width at half height is a maximum. From the computed $G_i(r)$, plotted in Fig. 2, we have found that both conditions are met for $G_8(r)$, so that we may conclude that $N_c \sim 8$. The calculation of the mean values r_i for each $G_i(r)$ gives a range of values going from $r_1 \approx 3.03$ Å to $r_8 \approx 4.0$ Å. Moreover, given the weak structure exhibited by $g(r)$ in the region corresponding to the shell of second-nearest neighbors, we have also plotted in Fig. 2 the corresponding $G_i(r)$. According to the previous criterion, this shell is composed of ten atoms, comprising from $G_9(r)$ to $G_{18}(r)$, with an associated range of values from $r_9 \approx 4.17$ Å to $r_{18} \approx 5.36$ Å. A more detailed analysis of the $G_i(r)$ allows to distinguish two subshells: one from $i=1$ to $i=4$, where the distance between the consecutive r_i is ≈ 0.1 Å, and a second group from $i=5$ to $i=8$, where the distances between the r_i's is ≈ 0.2 Å. Besides, for the first subshell, adding $G_1(r)$ up to $G_4(r)$, we find a mean value for the position $r_{\mathrm{sh},1} \approx 3.18$ Å and for the second one, which has four neighbors, $r_{\mathrm{sh},2} \approx 3.73$ Å. This substructure is reminiscent of the rhombohedral structure of the crystal, where the first coordination shell is decomposed into two subshells containing three atoms each, located at distances ≈ 3.1 Å, and ≈ 3.5 Å, respectively.

The bond angle distribution function $g_3(\theta)$ gives information about the distribution of bond angles defined by atoms up to a distance which we have taken as $R_{\min}=4.1$ Å. The calculated $g_3(\theta)$, shown in the inset of Fig. 2, exhibits two distinct peaks at $\sim 56°$ and 92°.

We have analyzed the correlations between the valence electrons and the Bi^{5+} ions. This is usually quantified by the electron-ion pair-distribution function $g_{ei}(\mathbf{r})$, defined as

$$g_{ei}(\mathbf{r})\rho_i n_0 \Omega = \left\langle \sum_{j=1}^{N} n(\mathbf{r}+\mathbf{R}_j) \right\rangle, \tag{1}$$

where ρ_i is the average ionic number density, $n(\mathbf{r})$ the valence electron density, n_0 the average electron density, $\mathbf{R}_j$ the ionic positions, and $\langle \cdots \rangle$ stands for the ensemble average. The ionic core is represented by a pseudopotential, so that the electronic charge density is only accurate outside this region. Nevertheless, the inaccuracy is limited to a region of about 0.7–0.8 Å around the atomic nucleus and has no consequences on the charge density at larger distances, especially in the region which is important for cohesive and structural properties. The computed $g_{ei}(r)$, which was obtained as an average over six configurations, is shown in Fig. 3. It has a marked peak at ≈ 0.9 Å; followed by rather weak oscillations. It practically coincides with that obtained by Wijs *et al.*,[19,20] except for the position of the main peak. Takeda *et al.*[36] have obtained an experimental $g_{ei}(r)$ from the differences between the values of $S(q)$ determined by XR and NS experiments. This is a very delicate task as it involves subtracting two very similar magnitudes and then taking its Fourier transform (FT), and their result is plotted in Fig. 3 for comparison. The experimental $g_{ei}(r)$ has a first peak whose position practically coincides with that of our AIMD calculations but this is the only common feature because the experimental data show strong oscillations.

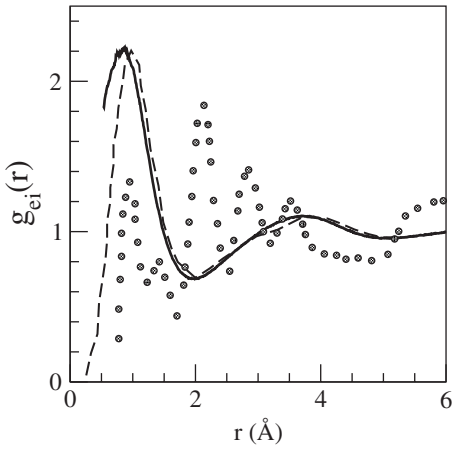

FIG. 3. Valence electron-ion pair-distribution function $g_{ei}(r)$ obtained in our AIMD simulation of *l*-Bi at 600 K (full line). Dashed line: AIMD results by de Wijs *et al.* (Refs. 19 and 20). Circles: experimental data at 573 K by Takeda *et al.* (Ref. 36).

B. Dynamic properties

1. Single-particle dynamics

The self-intermediate scattering function $F_s(\mathbf{q},t)$ describes the single-particle dynamics over different length scales, ranging from the hydrodynamic regime (small $\mathbf{q}$, long t) to the free-particle regime (large $\mathbf{q}$, short t). For homogeneous and isotropic systems, it depends only on $q=|\mathbf{q}|$ and is defined as $F_s(q,t)=\langle \exp[-i\mathbf{q}\cdot\delta\mathbf{R}(t)]\rangle$, where $\delta\mathbf{R}(t)=\mathbf{R}(t)-\mathbf{R}(0)$ and the average $\langle\cdots\rangle$ is over particles, time origins and wave vectors with the same modulus. The theoretical analysis of $F_s(q,t)$, and other time correlation functions, has usually been aided by the introduction of the corresponding memory functions, defined through the Volterra-type equation

$$\frac{dF_s(q,t)}{dt} = -\int_0^t d\tau M_s(q,\tau) F_s(q,t-\tau), \tag{2}$$

where $M_s(q,t)$ is the first-order memory function. The second-order memory function, $N_s(q,t)$, is defined as the first-order memory function of $M_s(q,t)$. The relations between the Laplace transforms of the corresponding functions are

$$\tilde{F}_s(q,z) = \frac{F_s(q,0)}{z+\tilde{M}_s(q,z)}, \quad \tilde{M}_s(q,z) = \frac{M_s(q,0)}{z+\tilde{N}_s(q,z)}, \tag{3}$$

which can be reiterated leading to a continued fraction representation of the functions. The initial ($t=0$) values in the numerators can be written in terms of the so-called frequency moments, which are related to the initial values of the even-order derivatives of the correlation function. These can be directly computed in a simulation run, because they can be expressed as averages of magnitudes involving atomic positions, velocities, and accelerations (and further derivatives for sixth or higher frequency moments).

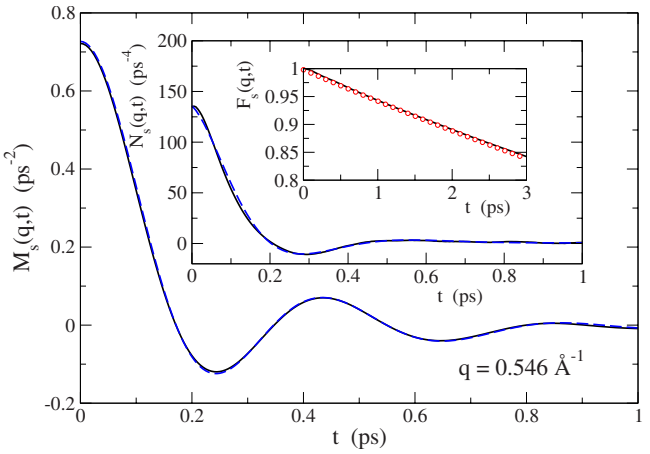

FIG. 4. (Color online) Full lines: $F_s(q,t)$ and the first- and second-order memory functions, as obtained from our AIMD simulations of *l*-Bi at 600 K. Dashed lines: functions obtained from the fit to the model specified in the text. Circles: real exponential component of the model for $F_s(q,t)$.

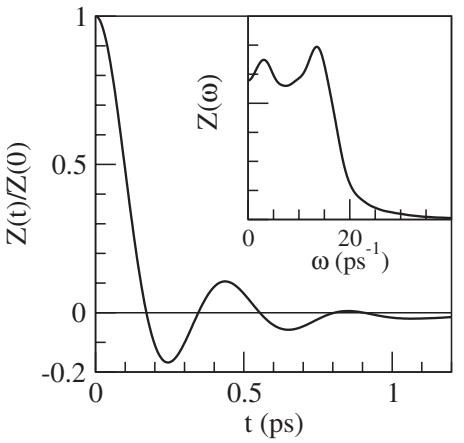

FIG. 5. Normalized velocity autocorrelation function $Z(t)/Z(0)$ obtained in our AIMD simulations of *l*-Bi at $T=600$ K. The inset shows the power spectrum $Z(\omega)$.

Within mode-coupling theories,[12] the second-order memory function is usually decomposed into several terms, each one related to a different relaxation mechanism for the magnitude under study. In this context, exponential functions play a prominent role due to their convenient analytical properties in the Laplace domain. Moreover, they can describe both monotonic or oscillating functions if real or complex exponents and amplitudes are considered (complex-conjugate pairs in the latter case). For instance, the viscoelastic scheme of Copley and Lovesey[37] assumes a single (real) exponential form for $N_s(q,t)$. On the other hand, the simplified mode-coupling approach of Gaskell and Miller[38] takes $M_s(q,t)$ as a sum of two contributions, one arising from couplings with longitudinal currents and the other from couplings with transverse currents. The former always leads to an oscillatory term, reflected in a high-frequency peak in the time FT of $M_s(q,t)$, whereas the latter turns into a low-frequency peak which, for some systems, can go to zero frequency. Using our AIMD results, we computed $F_s(q,t)$ and $M_s(q,t)$, and this latter was fitted to a sum of four exponential functions which, in principle, comprised two pairs of complex-conjugate terms corresponding to the high- and low-frequency components. The best fit was consistently obtained with the low-frequency equal to zero. In Appendixes A and B we specify more details about several technical aspects, such as the calculation of the memory functions, the analytical expression of the model, the constraints imposed, and the general form that $F_s(q,t)$ and $N_s(q,t)$ take within this model. Here, we just show the results for one q value (see Fig. 4) and pinpoint two consequences of the model. First, $F_s(q,t)$ is comprised of five exponentials, one of them real, which overwhelmingly dominates for small q values, and two pairs of complex-conjugate terms whose amplitudes are very small, but whose contribution at short times is essential to obtain a well-behaved $F_s(q,t)$. Second, $N_s(q,t)$ is comprised of three exponential functions, one real and a pair of complex-conjugate terms, i.e.,

$$N_s(q,t) = Ae^{-Bt} + e^{-Ct}[E\cos(Ft) + G\sin(Ft)]. \quad (4)$$

This represents a modification over the viscoelastic model and, as shown in Fig. 4, gives an excellent description of the AIMD results for *l*-Bi.

The velocity autocorrelation function (VACF) is defined as $Z(t)=\langle \mathbf{v}_a(t)\cdot\mathbf{v}_a(0)\rangle$, where $\mathbf{v}_a(t)$ is the velocity of a tagged ion in the fluid and angle-brackets indicate an ensemble average. The VACF can be also obtained from $Z(t) = \lim_{q\to 0} M_s(q,t)/q^2$. The first-order memory function of $Z(t)$ is therefore directly connected to $N_s(q,t)$ for $q\to 0$. Figure 5 shows the calculated $Z(t)$ along with its FT, $Z(\omega)$, known as the power spectrum. $Z(\omega)$ has a two-peaked shape. The expression used to model $M_s(q,t)$ leads, for $q\to 0$, to a similar formula for $Z(t)$, and consequently to an analytical expression for $Z(\omega)$, which reproduces the computed values. The high-frequency peak arises from the oscillatory term in Eq. (B1) of the Appendix B, while curiously the low-frequency peak arises from the opposite sign contribution of the two other terms that appear in the zero-frequency component of the model. $Z(t)$ exhibits the typical backscattering behavior with a clear first minimum and subsequent oscillations which are rather weak. This behavior is related to the so-called "cage effect," but whereas the closed-packed structure of SLMs yields a strong backscattering,[12] the more open structure of *l*-Bi ($N_c \approx 8$) induces a weaker cage effect and a dampening of the oscillations in $Z(t)$. An estimate of the frequency at which a given particle is vibrating within the cage can be achieved by the short-time expansion[39] $Z(t)=1-\omega_E^2 t^2/2+\cdots$, where ω_E is the so-called "Einstein frequency" of the system, whose value, obtained from the frequency moments, is $\omega_E=11.6$ ps^{-1}. For comparison, we mention that from the fourth frequency moment of the experimental dynamic structure factor and using some approximations, Dahlborg and Davidovič[6] and Dahlborg and Olsson[8] have obtained the values $\omega_E \sim 9.7$ ps and 13.0 ps^{-1}, respectively. Within the mode-coupling theory, and in the context of the previously mentioned approach of Gaskell and Miller[38] for $M_s(q,t)$, these authors developed a representation of $Z(t)$ as sum of two contributions arising from the coupling of the

single-particle motion to the collective longitudinal and transverse currents. Therefrom, the existence of a low-frequency (smaller than ω_E) peak in $Z(\omega)$ can be traced back to the transverse current component and is related to the ability of the liquid to sustain shear modes. On the other hand, the other peak appearing at the higher frequency (greater than ω_E) is shown to be a consequence of the coupling of the particle velocity to the longitudinal current. Some recent studies about the relative contribution of both components to $Z(\omega)$ have been performed in the case of liquid Si at different thermodynamic states.[40]

The self-diffusion coefficient D was found to be 0.191 ± 0.005 Å^2/ps when calculated by either the time integral of $Z(t)$ or from the slope of the mean square ion displacement function $r^2(t) \equiv \langle \delta \mathbf{R}(t)^2 \rangle$. There is some scatter in the reported experimental data at melting, namely, 0.167, 0.256, and 0.377 Å^2/ps.[41–43] Our predicted value agrees with the lowest experimental data (take into account the somewhat higher temperature of the simulations). Sani *et al.*[11] have recently estimated a value of D on the basis of their INS measurements of $S(q,\omega)$, whose quasielastic part was modeled in terms of two Lorentzian functions, one of them accounting for the diffusive process. From this scheme, they reached the value 0.167 Å^2/ps. The value obtained by de Wijs *et al.*[19,20] from their AIMD simulations of l-Bi at 1000 K was 0.3 Å^2/ps.

2. Collective dynamics

The collective dynamics of density fluctuations in liquids is usually described by means of the intermediate scattering function $F(q,t)$, defined as

$$F(q,t) = \frac{1}{N}\left\langle \left(\sum_{j=1}^{N} e^{-i\mathbf{q}\cdot\mathbf{R}_j(t+t_0)} \right)\left(\sum_{l=1}^{N} e^{i\mathbf{q}\cdot\mathbf{R}_l(t_0)} \right) \right\rangle, \quad (5)$$

where N is the total number of particles and $\mathbf{R}_j(t)$ is the position of the jth ion at time t. The FT of $F(q,t)$ into the frequency domain leads to the dynamic structure factor $S(q,\omega)$, which is directly related to the intensity of scattering in INS or inelastic XR experiments. Another important magnitude connected to the density fluctuations is the current due to the overall motion of the particles, defined as

$$\mathbf{j}(q,t) = \sum_{a=1}^{N} \mathbf{v}_a(t)\exp[i\mathbf{q}\cdot\mathbf{R}_a(t)], \quad (6)$$

which is usually split into a longitudinal component $j_L(q,t)$, parallel to $\mathbf{q}$, and a transverse component $j_T(q,t)$, perpendicular to $\mathbf{q}$. The longitudinal and transverse current correlation functions are obtained as

$$C_L(q,t) = \frac{1}{N}\langle j_L(q,t) j_L^*(q,0)\rangle \quad (7)$$

and

$$C_T(q,t) = \frac{1}{(2N)}\langle j_T(q,t) j_T^*(q,0)\rangle. \quad (8)$$

The corresponding time FTs give the associated spectra $C_L(q,\omega)$ and $C_T(q,\omega)$, with $C_L(q,\omega) = \omega^2 S(q,\omega)$. From the configurations generated in our AIMD simulations, we have calculated the above-mentioned dynamical properties of l-Bi at $T=600$ K, and those are reported below. The calculation of correlation functions of collective magnitudes suffers from poor statistics in comparison to one-particle properties because it is only possible to take one average for each configuration. This means that longer simulation runs are needed to obtain collective properties than single-particle properties. Moreover, if the dynamics of the system shows some kind of "nonsimple" behavior, even longer runs are needed. This has shown to be the case for liquid Bi, where we needed 8000 configurations in order to obtain well-converged results for the $F(q,t)$ functions at short and intermediate times. It is in these long runs that the efficiency of the PARSEC code in parallel computations shows its full potential. Nevertheless, the tails of some of the $F(q,t)$, especially those that decay more slowly, still show some noise.

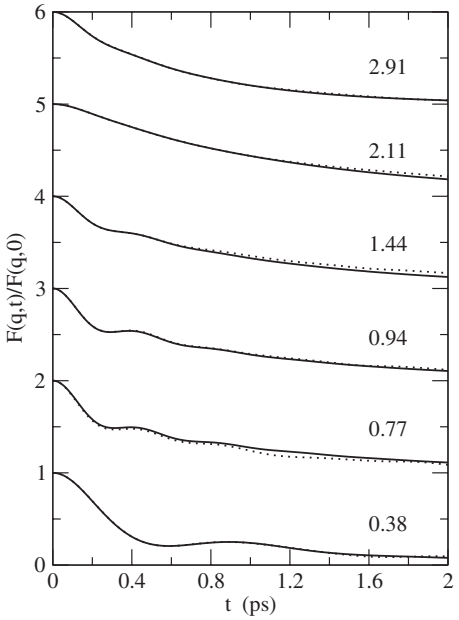

FIG. 6. Normalized intermediate scattering function $F(q,t)/F(q,0)$ of l-Bi at 600 K for several q values. Dotted lines: present AIMD results. Full lines: fittings of the AIMD results to the analytical model indicated in the text.

To analyze the mechanisms influencing the collective dynamics of l-Bi we have resorted again to the same theoretical approach used in the analysis of the single-particle dynamics, i.e., from the AIMD-derived $F(q,t)$ we have calculated its first- and second-order memory functions, $M(q,t)$ and $N(q,t)$, fitting $M(q,t)$ to a model similar to that used for $M_s(q,t)$; additional details are given in Appendix C. In passing, we note that this procedure also tackles adequately the remaining statistical noise of $F(q,t)$.

Figure 6 shows an illustrative sample of the computed $F(q,t)$ of l-Bi at $T=600$ K for several wave vectors. For $q \leq (3/5)q_p = 1.4$ Å^{-1}, $F(q,t)$ shows a damped oscillatory behavior superimposed on a strong diffusive component which yields a slow decay of this function. A similar diffusive behavior has been observed in other liquid metals such as l-Si,[32] l-Ge,[44] l-Sn,[33] l-Pb,[45] and l-Hg.[46] On the contrary, for SLMs (liquid alkalis, alkali earths, and Al) near melting and

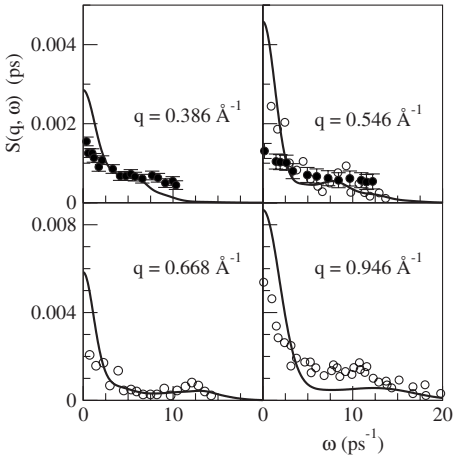

FIG. 7. Full lines: dynamic structure factor $S(q,\omega)$ obtained in our AIMD simulations of *l*-Bi at $T=600$ K for several q values. Full circles: experimental INS data at 580 K from Sani *et al.* (Ref. 11). Open circles: experimental INS data at 673 K from Shibata *et al.* (Ref. 10).

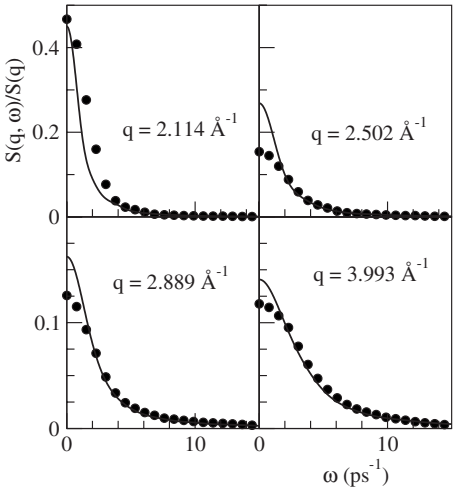

FIG. 9. Full lines: normalized dynamic structure factor $S(q,\omega)/S(q)$ obtained in our AIMD simulations of *l*-Bi at $T=600$ K for several q values. Full circles: experimental INS data at 583 K from Dahlborg and Olsson (Ref. 8).

for an equivalent q range, the diffusive component is weak and the associated $F(q,t)$ displays marked oscillations around zero.[47–53] We note that this behavior of the AIMD $F(q,t)$ for *l*-Bi is very different from that derived from CMD simulations,[18] where large oscillations and even negative values were found for $F(q,t)$. This discrepancy underlines some of the limitations inherent to an interatomic pair-potential model of *l*-Bi, even if the pair potential is constructed so as to reproduce the experimental static structure factor. Figure 6 provides a comparison between our AIMD results for $F(q,t)$ and the curves obtained by fitting them to the analytical model. Notice that the main effect of the fitted curves is to impose, for intermediate and long times, a smooth decay on $F(q,t)$.

From the computed $F(q,t)$, we have calculated the spectra $S(q,\omega)$ by direct numerical time FT and by resorting to the analytical time FT of the model, both routes leading to very similar results. Figures 7–9 show the calculated $S(q,\omega)$ for several values of q, together with the INS experimental data.[8,10,11] We observe side peaks, indicative of collective density excitations, up to $q\approx(3/5)q_p\approx 1.4$ Å^{-1}, and for greater q values $S(q,\omega)$ shows a monotonic decreasing behavior. Although there is qualitative agreement between

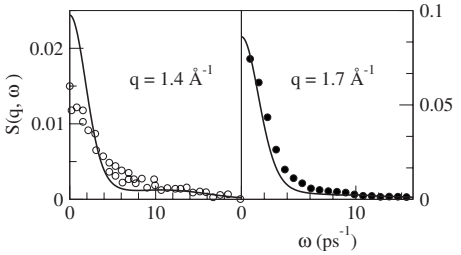

FIG. 8. Full lines: dynamic structure factor $S(q,\omega)$ obtained in our AIMD simulations of *l*-Bi at $T=600$ K for several q values. Open circles: experimental INS data at 673 K from Shibata *et al.* (Ref. 10). Full circles: experimental INS data at 583 K from Dahlborg and Olsson (Ref. 8).

simulations and experiments, some discrepancies are visible, especially in the contact values $S(q,0)$. We note, however, that there are noticeable disagreements among the different sets of experimental data. Specifically, in the INS measurements of Dahlborg and Olsson[8,9] side peaks in $S(q,\omega)$ were found for $q\leq 0.6$ Å^{-1} only, whereas in the INS measurements by Shibata *et al.*[10] they were found up to $q=1.2$ Å^{-1}. Moreover, the comparison between the INS data of Shibata *et al.*[10] and Sani *et al.*[11] for $S(q,\omega)$ at $q=0.6$ Å^{-1} shows notable differences, specially for the contact value.

The INS measurements of Sani *et al.*[11] for *l*-Bi at $T=580$ K allowed to determine $S(q,\omega)$ within the range $0.15\leq q\leq 0.6$ Å^{-1}. These results were analyzed by modeling $S(q,\omega)$ in terms of two Lorentzian functions to describe the quasielastic part and a damped harmonic oscillator (DHO) to account for the purely inelastic part. Their results for the inelastic term revealed the existence of propagating collective excitations. By identifying the DHO frequency to that of the inelastic peaks, a dispersion relation $\omega_l(q)=qc_s(q)$ was obtained, in which $c_s(q)$ is a q-dependent sound velocity and $\omega_l(q)$ is the frequency at which the longitudinal current correlation function $C_L(q,\omega)=\omega^2 S(q,\omega)$ attains its maximum. Their calculated values for $c_s(q)$ change from $\approx 1680\pm 80$ m/s (at $q\to 0$) to a maximum of $\approx 2005\pm 120$ m/s (at $0.3\leq q\leq 0.6$ Å^{-1}). This value implies a significant "positive dispersion effect," i.e., an increase with respect to the hydrodynamic adiabatic velocity value, of $\approx 20\%$, which is in line with the values already found for other liquid metals[12,13] (the experimental adiabatic sound velocity of *l*-Bi at melting is ≈ 1640 m/s; Ref. 54).

We have evaluated a dispersion relation, shown in Fig. 10, for the density fluctuations using the positions, $\omega_m(q)$, of the side peaks of our AIMD results for $S(q,\omega)$, obtained as the numerical FT of the $F(q,t)$ functions. Unfortunately, the small size of the simulation box implies that the smallest attainable q value ($q_{\min}=0.386$ Å^{-1}) is not small enough to allow a precise quantitative estimate of $c_s(q\to 0)$. However, an approximated value may be extracted from the position of

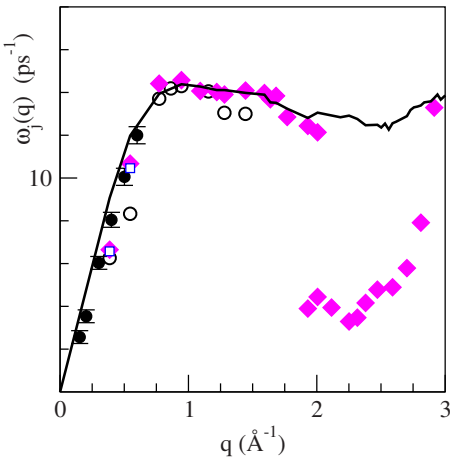

FIG. 10. (Color online) Dispersion relation for *l*-Bi at 600 K, as obtained from our AIMD calculations from the positions of the inelastic peaks in $S(q,\omega)$ (open circles) and from the maxima in the spectra of the longitudinal current $C_L(q,\omega)$ (diamonds). The filled circles with error bars are the INS data from Sani *et al.* (Ref. 11). The open squares are the results of fitting the inelastic line of the AIMD $S(q,\omega)$ to the model used by Sani *et al.* (Ref. 11). The line shows the values of $\omega_L(q)$.

the side peak in $S(q_{\min},\omega)$, which gives $c_s(q_{\min}) = 1620 \pm 150$ m/s. Moreover, our results also point to some positive dispersion effect in our calculated dispersion relation with a maximum of $\approx 2070 \pm 150$ m/s at $q \approx 0.65$ Å^{-1}. It is interesting to note the rather flat shape of the dispersion for q values between 0.75 and 1.4 Å^{-1}.

To properly compare our results with Sani *et al.*'s experimental data,[11] we have determined the dispersion relation from the maxima of $C_L(q,\omega)$, as obtained by our AIMD simulations. Thus, we have derived a relation $\omega_l(q)$ which closely follows Sani *et al.*'s results, as it can be seen in Fig. 10. We have also plotted in this figure the results obtained for $\omega_L(q) = \sqrt{\omega^{(4)}(q)/\omega^{(2)}(q)}$ from the frequency moments. For small q it goes linearly to zero, and its slope is called the "infinite frequency" speed of sound, which is usually close to the maximum velocity associated to the positive dispersion effect. Note that the flatness of the dispersion indicated above is already present at the level of $\omega_L(q)$. The estimate for the positive dispersion and the value $c_s(q_{\min}) = 1750 \pm 100$ m/s are similar to the data of Sani *et al.*[11] It may be noted that in a small q range around 2.0 Å^{-1} two peaks appear in $C_L(q,\omega)$. In fact, there is a larger q region surrounding this one where $C_L(q,\omega)$ shows a peak and a shoulder, although Fig. 10 only displays the positions of the peaks. We have also used the same model as Sani *et al.*[11] to fit the inelastic component of our calculated $S(q,\omega)$. The results for the frequency virtually coincide with the maxima in $C_L(q,\omega)$.

Sani *et al.*[11] have also reported the ratio between the damping rate and the frequency obtained from their fit, with values between 0.4 and 1.1, while other polyvalent metals show ratios between 0.3 and 0.6. In order to find the origin of this unique feature of *l*-Bi we must first analyze the different terms that contribute to $F(q,t)$.

To this end, it would be very useful to apply some theory that enables disentangling their physical origin. For instance, for small q values the hydrodynamic theory,[39] using as variables the conserved ones, i.e., the density, the longitudinal current, and the energy density, explains the main features of $F(q,t)$ and the origin of the "modes" that contribute to them, namely, sound propagation and thermal diffusion. For greater q values other variables, besides the hydrodynamic ones, start to contribute to the behavior of the correlation functions. Some theories, such as the generalized collective modes (GCM) approach,[55] through the inclusion of nonconserved variables, allow the extension of the hydrodynamic formalism outside the small q regime, and then, through the evaluation of eigenvalues of a generalized hydrodynamic matrix, find the time dependence of the different modes that contribute to the correlation functions, and, from the corresponding eigenvectors, their strength and physical origin. In principle, the GCM approach can be used with an arbitrary number of dynamic variables, which may or may not include all the hydrodynamic ones. For instance, using the density, the longitudinal current, and the time derivative of the longitudinal current (and excluding the energy density) leads to the so-called viscoelastic model. These variables are determined only by the positions, velocities, and accelerations of the particles, so they are readily available from any MD run. Also, higher derivatives have been considered in specific applications. However, the inclusion of the energy density, its time derivative, and sometimes also higher-order derivatives is usually required in order to obtain a good agreement between the results of the GCM model and the numerically computed ones. The evaluation of these variables, in the present formulation of the theory, requires to assign an energy to each particle of the system; this is easily done for systems whose particles interact through pairwise additive potentials, but it is not possible for systems whose potential energy depends globally on all of the atomic positions, as is the case of *ab initio* MD simulations. So, although physically appealing, the most general GCM approach cannot be used for the analysis of our simulation results.

Notwithstanding this, it is known that an n-variable GCM model leads to a mathematical expression of $F(q,t)$ as a sum of n exponential functions. Therefore, our fitting model (see Appendix C) is mathematically equivalent to a five-variable GCM approach. Of course, fitting precludes the direct determination of the physical origin of the different modes appearing in the behavior of the correlation functions, as even the dynamic variables are not specified, but it does enable the calculation of the time dependence and strengths of these modes. It is only through comparison with the results of simplified models, or with the known behavior of the different modes in other systems, that one can *suggest* the origin of the modes found in the fitting process.

Figure 11 shows the damping rates of the different modes appearing in the analytical expression of our model $F(q,t)$, as well as the corresponding frequencies, and Fig. 12 shows the amplitudes of these modes. The largest amplitude and smallest decay rate correspond to a diffusionlike term that, therefore, dominates the overall slowly decaying shape of $F(q,t)$. Moreover, it attains a maximum strength at q values near the main peak of $S(q)$; this is the typical behavior of a structural relaxation mode.

Concerning the propagating modes, there is a high-frequency one in the whole q range, while a low-frequency

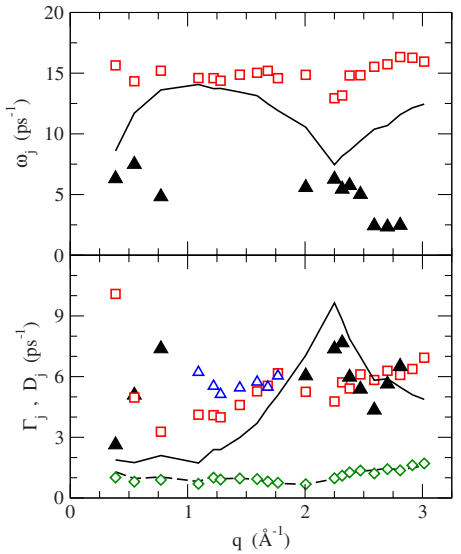

FIG. 11. (Color online) Frequencies and damping rates of the different modes of $F(q,t)$. Diamonds: slow diffusionlike mode. Squares: high-frequency propagating mode. Filled triangles: low-frequency propagating mode. Open triangles: fast diffusionlike mode. Continuous lines: results for the GCM viscoelastic propagating mode. Dashed line: results for the GCM viscoelastic structural relaxation mode.

mode, present at small q and near the main peak of $S(q)$, disappears in the region $1 \leq q \leq 2$ Å^{-1}, where it is replaced by a diffusionlike mode. Notice that when only one propagating mode exists, it has a larger amplitude than the diffusivelike term. However, when the low-frequency mode exists, it dominates over the high-frequency one. This is the case for $q \to 0$, where we observe that the amplitude of the high-frequency mode becomes very small, which is a signature of a kinetic (nonhydrodynamic) mode.

The overall picture of frequencies and damping rates as a function of q is rather different from the picture usually observed for one-component liquids. In those cases where a five-variable GCM analysis has been performed,[56] it has been shown that in the hydrodynamic limit one should find

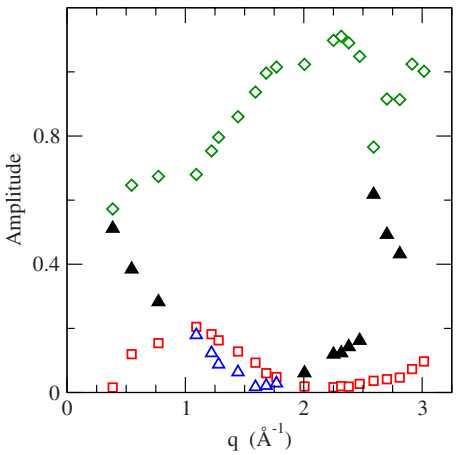

FIG. 12. (Color online) Amplitudes of the different modes of $F(q,t)$. The symbols have the same meaning as in Fig. 11.

the hydrodynamic modes (sound propagation and thermal diffusion) and two more kinetic diffusionlike modes: the structural relaxation mode and another heat relaxation mode. This behavior is certainly not found in our data. But this simply means that the hydrodynamic regime is far from being accessible to our simulations. For larger q values, the five-variable GCM model has been found to lead to two propagating modes (sound and heat waves) and the structural relaxation mode.[56] This is the kind of behavior we observe in liquid Bi, except in the region between 1 and 2 Å^{-1}, where there is a "propagation gap" for one of the modes. Nevertheless, the obtained wave-vector variation in the frequencies, in particular, its flatness, is also quite different from that found for the systems where sound and heat waves have been explicitly identified with the GCM model. In order to shed some more light into the problem, we have made a GCM viscoelastic calculation. It is known that this model leads to a structural relaxation mode and a propagating mode, akin to sound propagation.[57] These results are also shown in Fig. 11. We observe that in the whole q range the "viscoelastic structural relaxation" damping rate is very close to the one found in the fitting procedure, thus buttressing the interpretation of the latter as a structural relaxation mode. In the q region between 0.75 and 1.8 Å^{-1} the "viscoelastic sound" mode is close to our high-frequency one, both in frequency and damping rate, being also quite flat with respect to wave-vector variation. We therefore suggest that in this q range our high-frequency mode is dominated by density fluctuations, behaving like "typical" sound propagation in other liquids. Outside this region, and, in particular, for $q \leq 0.6$ Å^{-1}, there is an important coupling with other variables (the energy density being an obvious candidate) that leads to the appearance of two propagating modes, and makes the behavior of $F(q,t)$ in this q regime rather more complex than in other liquid metals, which is indeed consistent with the experimental findings of Sani *et al.*[11]

The ratios between the damping rates and the frequencies of these two propagating modes found from our analysis are shown, together with Sani *et al.*'s data, in Fig. 13. We recall that the low-frequency mode dominates in the low-q region, where we observe that our model produces even larger ratios than the experiment. However, for larger q, where the high-frequency mode dominates and the low-frequency mode disappears, the damping ratio is rather q independent, with values around 0.4–0.6, quite in line with other polyvalent metals. We note that if we fit our results to the model used by Sani *et al.*, we obtain basically the same values as they did. The reason for the difference between our results for the dominating low-frequency mode ratio and those of the fit to the model of Sani *et al.* lies in the neglect of a frequency-dependent term in their model (see Appendix C), which leads to an effective damping rate smaller than the real one.

The nature of the different relaxation mechanisms for the density fluctuations that finally lead to $F(q,t)$ is analyzed through the behavior of the different terms appearing in the second-order memory function $N(q,t)$. In the hydrodynamic region $(q \to 0)$, the linearized hydrodynamic theory states that $N(q,t)$ is comprised of a slowly decaying exponential term, due to thermal relaxation, and an instantaneous Dirac delta term related to viscous relaxation. An extension of this

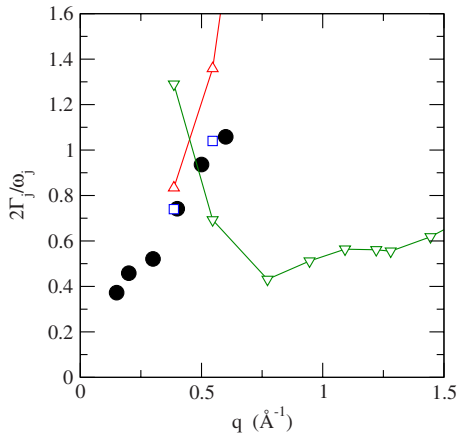

FIG. 13. (Color online) Damping ratio $2\Gamma_j/\omega_j$ as obtained by Sani *et al.* (Ref. 11) (circles), from the high-frequency mode (down triangles), from the low-frequency mode (up triangles), and from the fit of our AIMD data to the model used by Sani *et al.* (Ref. 11) (squares).

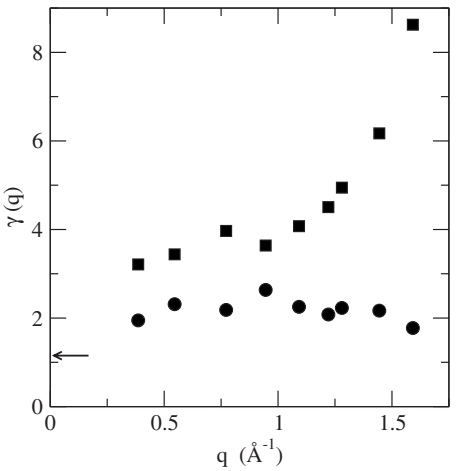

FIG. 14. Circles: $\gamma(q)$ values obtained by assigning a thermal origin to the slow relaxation channel in $N(q,t)$. Squares: values obtained by assigning a viscoelastic origin to the slow relaxation channel. The arrow indicates the thermodynamic value of γ.

model to larger q values leads to the so-called "generalized hydrodynamic theory," where the different thermophysical parameters become q dependent, and where the instantaneous viscous relaxation is substituted by a viscoelastic fast decaying exponential. In the case of liquid metals, there is some debate on whether or not the thermal relaxation term should include the contribution of the valence electrons to the thermal diffusivity. Indeed, the generalized hydrodynamic picture has been challenged for the case of liquid metals, where the full thermal diffusivity is very high, so that thermal relaxation becomes the fast decaying channel and the viscoelastic relaxation turns out to be the slow mechanism.[13] This does not alter the general shape of the dynamic structure factor for small q, where a quasielastic and an inelastic line still appear, but relates the damping of the quasielastic line to viscoelastic magnitudes and not to the thermal diffusivity. Some support for this idea has recently been provided by some AIMD simulations of *l*-Hg near melting.[46] However, *l*-Bi is not a "good" metal (in the solid phase it is, in fact, a semimetal), and this means a lower thermal diffusivity. Therefore, it is interesting to analyze if the thermal relaxation is the fast or the slow channel. As we show in Appendix C, the model we are using leads to an $N(q,t)$ with a slow exponential term and a fast component which, however, can be composed of two real exponentials, one real exponential and a Dirac delta term, or a fast decaying damped oscillatory term, depending on the q range (in the particular case of small q, the latter is found). In the generalized hydrodynamic picture, the amplitude of the slow channel is related to the generalized specific heat ratio $\gamma(q)$ [which for $q \to 0$ becomes $\gamma = C_p/C_v$, as specified in Eq. (C4) of Appendix C]. On the other hand, if the slow channel is associated to viscoelastic relaxation the relation between its amplitude and $\gamma(q)$ is different, as given in Eq. (C5). Figure 14 shows the q dependence of $\gamma(q)$ obtained from both possibilities. Few direct calculations of $\gamma(q)$ from the hydrodynamic time correlation functions are available in the literature. For the particular case of liquid metals, we are only aware of results for *l*-Bi,[18] *l*-Li,[58] and *l*-Pb,[59] obtained from CMD simulations. The picture yielded by these calculations was that $\gamma(q)$ starts at the thermodynamic value of γ for $q=0$, then decreases to values near 1, and finally increases only in the region around q_p. The thermodynamic value of γ for *l*-Bi at melting, shown in Fig. 14 with an arrow, is 1.15. According to this figure, the assumption of relating the slow relaxation channel to thermal relaxation seems most plausible. First, because it can be extrapolated smoothly to the thermodynamic value, and second because the variation with q, even if different from that found from pair potential studies, does not show a large increase at intermediate q values, but remains rather constant. So, within the limitations imposed by the fact that the smallest q value attainable in the simulations is not really very small, that the simulation time is long for standard AIMD but short for standard CMD simulations, and especially by the fact that we are modeling and not making direct calculations of $\gamma(q)$, our results suggest that in the case of *l*-Bi thermal relaxation is the slow channel, which is different from the results obtained by AIMD simulations of *l*-Hg (Ref. 46) and from the analysis of some experimental measurements of other liquid metals.[13]

The transverse current correlation function, $C_T(q,t)$, is not directly linked to any measurable quantity, but it can be determined by means of computer simulations or some theoretical model. It gives information on the shear modes and its spectrum, $C_T(q,\omega)$, when plotted as a function of ω, may show peaks within some q range, which are connected with propagating shear waves. This is shown in Fig. 15 which depicts both correlation functions for a wide range of q values. The $C_T(q,\omega)$ display peaks for a wide range, namely, $0.2q_p \leq q \leq 3.0q_p$, which is comparable to what has been found in SLMs.[12] In passing we note that there is no peak for the smallest attainable q, namely, $q=0.386$ Å^{-1}. The shear viscosity coefficient η can be calculated from $C_T(q,t)$ and details of the method are given in Refs. 12 and 47. Our AIMD calculations lead to the value $\eta=1.70\pm0.10$ GPa ps. The experimental value for *l*-Bi at melting ($T=544$ K) is $\eta=2.10\pm0.02$ GPa ps,[60] which when extrapolated[60] to the temperature used in the present study, $T=600$ K, gives $\eta=1.78\pm0.02$ GPa ps.

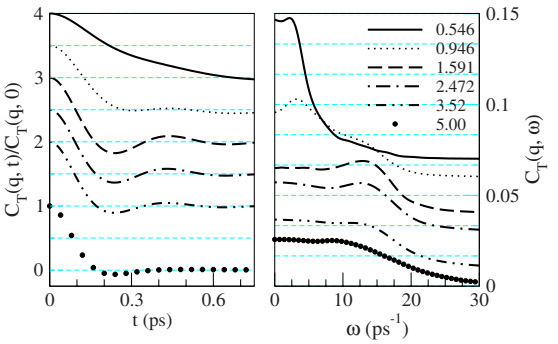

FIG. 15. (Color online) Transverse current correlation function $C_T(q,t)$ and its spectra $C_T(q,\omega)$ for *l*-Bi at 600 K, at several q values (in $Å^{-1}$).

Within the context of the Brownian motion of a macroscopic particle of diameter d in a liquid of viscosity η, the Stokes-Einstein relation $\eta D = k_B T/2\pi d$, where k_B is the Boltzmann constant, provides a connection between η and the self-diffusion coefficient D. Although approximate when applied to atoms, this relation has been used to estimate η (or D) by identifying d with the position of the main peak of $g(r)$. The present calculations give $d=3.30$ Å, which combined with our AIMD value $D=0.191$ $Å^2/ps$ leads to an estimate $\eta=2.09$ GPa ps. Although this result is somewhat larger than that obtained above, it still supports the validity of using the Stokes-Einstein relation for atoms.

C. Electronic properties

Figure 16 shows the single-particle electronic DOS computed for *l*-Bi at $T=600$ K and its angular momentum decomposition in *s*, *p*, *d*, and *f* channels. The DOS shows a strong deviation from the free-electron parabolic curve, having two bands below the Fermi level with dominant *s* (lower-band) and *p* (upper-band) characters. Such bands are separated by an energy gap of ≈3.5 eV. This result, which agrees with that obtained by Hafner and Jank[17] using an orthogonalized-plane-wave pseudopotential, is in marked

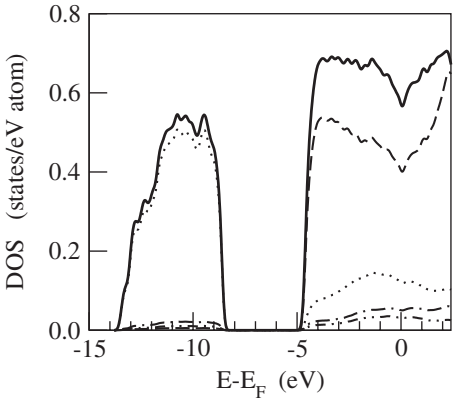

FIG. 16. DOS for *l*-Bi at 600 K as obtained from our AIMD calculations (solid lines). The angular momentum decomposition of the DOS in the *s* (dotted line), *p* (dashed line), *d* (dot-dashed line), and *f* (double dot-dashed line) channels is also shown.

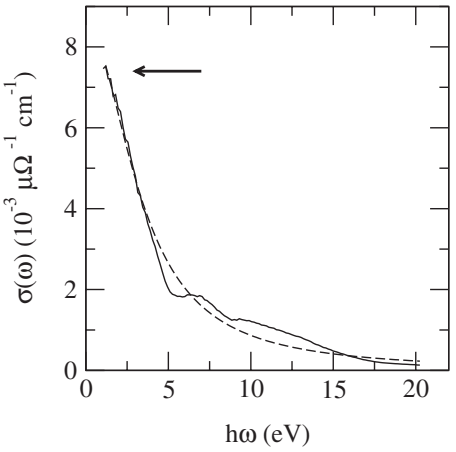

FIG. 17. Electrical conductivity of *l*-Bi at 600 K as computed from the real-space approach employed in this work by using the Kubo-Greenwood formula. The conductivity has been averaged over five ionic configurations and four **k** points of the simple cubic Brillouin zone. The arrow represents the experimental value obtained for *l*-Bi at 673 K (Ref. 62). The dashed line represents the Drude curve fitted to the computed values for the conductivity (see the text).

contrast with the nearly free-electron parabola exhibited by SLMs.[53]

Within the real-space formalism employed in this work, we have also computed the electrical conductivity $\sigma(\omega)$ of *l*-Bi using the Kubo-Greenwood formula[61]

$$\sigma(\omega,\{\mathbf{R}_a\}) = \frac{2\pi e^2}{3m_e^2\Omega\omega}\sum_{i,j}(f_i - f_j)|M_{ij}|^2\delta(E_j - E_i - \hbar\omega), \tag{9}$$

where Ω is the volume of the simulation box, m_e is the electron mass, E_n is the eigenvalue for the nth state with occupancy number f_n, $\{\mathbf{R}_a\}$ is the ionic configuration of the liquid, and M_{ij} is the matrix element of the momentum operator between the single-particle eigenvectors ψ_i and ψ_j, i.e., $M_{ij}=\langle\psi_i|\hat{p}|\psi_j\rangle$. Equation (9) was computed using several **k** points of the simple cubic Brillouin zone using the expression

$$\sigma(\omega) = \sum_{\mathbf{k}} \sigma(\omega,\mathbf{k})w(\mathbf{k}), \tag{10}$$

where $w(\mathbf{k})$ is the weight of each of the **k** points.

The conductivity must satisfy the following sum rule (that is a generalization of the sum rule of the oscillator strength)

$$S = \frac{2m_e\Omega}{\pi e^2 N_e}\int_0^\infty \sigma(\omega)d\omega = 1, \tag{11}$$

where N_e is the total number of the electrons of the system. The value of S for the computed conductivity is smaller than 1 ($S\approx 0.95$) since the calculation is performed for a finite number of states. The dc conductivity is the value of $\sigma(\omega)$ at zero frequency. As it can be seen in Fig. 17, the computed frequency-dependent conductivity is well compatible with

the experimental dc conductivity value of 7.4×10^{-3} $\mu\Omega^{-1}$ cm^{-1}.[62]

It has been shown[53] that for SLMs the conductivity fits very well the Drude-type function for free electrons

$$\sigma(\omega) = \frac{\sigma}{1 + \omega^2\tau^2}, \tag{12}$$

where τ is the relaxation time and σ is the dc conductivity. In contrast, the computed conductivity for *l*-Bi does not show a Drude-type behavior (see Fig. 17). For example, the conductivity has a significative hump centered around at 7 eV which is related to the energy gap of 3.5 eV that appears in the DOS below the Fermi level (from −5 to −8.5 eV, see Fig. 16); indeed, the lack of states in this gap prevents any transition from the states within this energy range to unoccupied states above the Fermi level.

IV. SUMMARY AND CONCLUSIONS

We have reported a comprehensive study of the static, dynamic, and electronic properties of *l*-Bi in a thermodynamic state near its melting point. The study has been performed by means of 124-atom AIMD simulations based on PARSEC,[21,23] a real-space pseudopotential approach based on DFT. The conclusions of our AIMD study can be summarized as follows.

(i) The results for the static structure factor $S(q)$ and the pair-distribution function $g(r)$ are in good agreement with the available experimental data.[5–7] They confirm that the structure of *l*-Bi has some features reminiscent of the rhombohedral structure of the crystal, where the first coordination shell is decomposed into two subshells, each one containing four atoms.

(ii) The computed first-order memory function of the self-intermediate scattering function $F_s(q,t)$, which we analyze within the framework of the mode-coupling ideas, is fitted to an analytical expression which generalizes the well-known viscoelastic model and provides a good description of the computed $F_s(q,t)$. Moreover, it reproduces the double-peak structure exhibited by the power spectrum of the velocity autocorrelation function, $Z(\omega)$.

(iii) The calculated intermediate scattering function $F(q,t)$ shows at low-q values a strong diffusive component which imposes a slow decay. The corresponding dynamic structure factor $S(q,\omega)$ is in fair agreement with the INS experimental data.[8–11] In particular, $S(q,\omega)$ exhibits side peaks, which are indicative of collective density excitations, over a range of wave numbers up to $q \approx 1.4$ Å^{-1}, in keeping with the experimental data of Shibata *et al.*[10] Moreover, our AIMD simulations suggest an important positive dispersion effect of the density fluctuations of around 20%, which is similar to the estimate made by Sani *et al.*[11] from their INS measurements.

(iv) We have explained the peculiar magnitude of the experimental width of the inelastic peak in $S(q,\omega)$ for $q < 0.6$ Å^{-1} as being related to the existence and behavior of two propagating modes in this wave-vector region. For larger q, only one of the modes survives and the damping turns to behave in a similar way to other polyvalent metals.

(v) By analyzing the relaxation mechanisms for the density fluctuations on the basis of the different contributions to the second-order memory function of $F(q,t)$, we suggest that the thermal relaxation is the slow decaying channel, whereas the viscoelastic relaxation is the fast decaying channel. This is just the opposite of what has been found in some liquid metals[13,46] and may be attributed to the semimetal character of Bi.

(vi) The spectra of the transverse current correlation functions $C_t(q,\omega)$ has inelastic peaks within a wide q range.

(vii) Most static and dynamic properties of *l*-Bi show different trends from those typical of SLMs. Only the VACF and the transverse currents show more similarities because these properties are mainly determined by the short-range order as quantified by the number of nearest neighbors. Liquid Bi has ≈8 nearest neighbors, which is somewhat smaller than the ≈10–12 neighbors typical of SLMs but it is not small enough to induce qualitative changes in those properties.

(viii) The predicted values of the self-diffusion, adiabatic sound velocity, and shear viscosity are in good agreement with experimental data.[41,54,60]

(ix) The computed DOS curve shows a strong deviation from the free-electron parabolic curve, with two bands below the Fermi level with dominant *s* and *p* characters separated by an energy gap of 3.5 eV, in marked contrast with the behavior of SLMs such as *l*-Al.[53] The predicted electrical conductivity of *l*-Bi is in good agreement with the experimental data.[62]

ACKNOWLEDGMENTS

This work was supported by the Spanish Ministry of Science and Innovation in conjunction with the European Regional Development Fund (Grants No. FIS2008-02490/FIS and No. FIS2008-04894/FIS and Program "Ramón y Cajal"), the Junta de Castilla y León (Grants No. VA068A06 and No. GR120), the Directorate General for $R+D+i$ of the Xunta de Galicia (Grants No. INCITE09E2R206033ES and No. INCITE08PXIB206107PR), and the Consellería de Educación e Ordenación Universitaria de la Xunta de Galicia/FEDER (Axudas para a Consolidación e Estruturación de Unidades de Investigación Competitivas do SUG). Facilities provided by the Galician Supercomputing Centre (CESGA) are also acknowledged.

APPENDIX A: CALCULATION OF MEMORY FUNCTIONS

The calculation of the memory function through a direct application of Eq. (2) suffers from numerical instability, so that small errors in the memory function for short times increase rapidly for larger times. These problems are related to the use of numerical derivatives. Here we show how to circumvent them leading to a numerically stable procedure. We rewrite Eq. (2) as

$$\dot{F}(x) = -\int_0^x d\tau M(\tau)F(x-\tau). \tag{A1}$$

Integrating with respect to x from 0 to t, we get

$$F(t) - F(0) = -\int_0^t dx \int_0^x d\tau M(\tau) F(x-\tau)$$
$$= -\int_0^t d\tau \int_\tau^t dx M(\tau) F(x-\tau) =$$
$$-\int_0^t d\tau M(\tau) \int_0^{t-\tau} du F(u)$$
$$= -\int_0^t d\tau M(\tau) Y(t-\tau). \quad \text{(A2)}$$

In a simulation $F(t)$ is obtained at equidistant times $t_n = n\delta t$. From this, its integral $Y(t_n)$ is readily evaluated. Usually, the initial value of the memory function $M(0)$ is known; otherwise, it can be estimated from the numerical second derivative of $F(t)$ at $t=0$. Finally, discretization of the integral in Eq. (A2) leads to a set of equations for $M(t_n)$ that can be solved recursively in a straightforward way.

APPENDIX B: FITTING MODEL FOR THE SINGLE-PARTICLE DYNAMIC PROPERTIES

The equations relating the Laplace transforms of F_s and the memory functions include the $t=0$ values of these functions (we drop the q dependence where it is not essential). These are obtained from the frequency moments as $F_{s,0} \equiv F_s(q,0) = \omega_s^{(0)}$, $M_{s,0} \equiv M_s(q,0) = \omega_s^{(2)}/\omega_s^{(0)}$, and $N_{s,0} \equiv N_s(q,0) = \omega_s^{(4)}/\omega_s^{(2)} - \omega_s^{(2)}/\omega_s^{(0)}$. The expressions for these moments are: $\omega_s^{(0)} = 1$, $\omega_s^{(2)}(\mathbf{q}) = \langle (\mathbf{q}\cdot\mathbf{v})^2 \rangle = (k_B T/m) q^2$, $\omega_s^{(4)}(\mathbf{q}) = \langle (\mathbf{q}\cdot\mathbf{v})^4 + (\mathbf{q}\cdot\mathbf{a})^2 \rangle = \omega_s^{(2)}(3\omega_s^{(2)} + \omega_E^2)$, where $\mathbf{v}$ and $\mathbf{a}$ denote the particle's velocity and acceleration, k_B is Boltzmann's constant, m is the particle's mass, and ω_E is the Einstein frequency. The averages are readily obtained from the simulation, so the initial values of the memory functions are known.

As explained in the main text, $M_s(q,t)$ is fitted to a sum of four exponentials, including a pair of complex-conjugate terms of high frequency and two more functions which are the limit of the complex-conjugate terms for zero frequency, namely,

$$M_s(q,t) = e^{-g_1 t}[a_1 \cos(\epsilon t) + b_1 \sin(\epsilon t)] + e^{-g_2 t}[a_2 + b_2 t]. \quad \text{(B1)}$$

Imposing the values of $M_{s,0}$, $\dot{M}_s(q,0) = 0$, and $\ddot{M}_s(q,0) = -M_{s,0}N_{s,0}$, we end up with four free parameters (in particular, we use g_1, g_2, ϵ, and a_1). The Laplace transform reads

$$\tilde{M}_s(q,z) = \frac{a_1(z+g_1) + b_1\epsilon}{\epsilon^2 + (z+g_1)^2} + \frac{a_2}{z+g_2} + \frac{b_2}{(z+g_2)^2}, \quad \text{(B2)}$$

which can be rewritten as $\tilde{P}_3(z)/\tilde{P}_4(z)$, where $\tilde{P}_n(z)$ denotes a polynomial of degree n. Taking this expression to Eq. (3), it is noticed that $\tilde{F}_s(q,z) = \tilde{P}_4(z)/\tilde{P}_5(z)$ and $\tilde{N}_s(q,z) = \tilde{P}_2(z)/\tilde{P}_3(z)$, so that after a partial fraction decomposition and inverse Laplace transformation we get $N_s(q,t)$ and $F_s(q,t)$ as a sum of three and five exponential functions, respectively. The exponents must appear as real or in pairs of complex-conjugate terms. In all cases, we have obtained one real and two pairs of complex-conjugate terms for $F_s(q,t)$, and one real and a pair of complex-conjugate terms for $N_s(q,t)$, as expressed in Eq. (4). Note that by imposing the value of $N_s(t=0) = N_{s,0}$ and a zero-frequency root in $M_s(q,t)$, Eq. (4) turns into a four-parameter expression.

Finally, the time FT of $M_s(q,t)$ can be obtained as $M_s(q,\omega) = \mathrm{Re}[\tilde{M}_s(q, z=i\omega)]/\pi$. The first term in Eq. (B2) leads to a typical stretched Lorentzian side peak at a frequency near ϵ. The other two terms lead to lines centered at $\omega=0$, one of them Lorentzian in shape and the other given as a squared Lorentzian. In all cases, the Lorentzian turned out to have a positive coefficient and the squared Lorentzian a negative coefficient with a combined net effect of a peak in $M_s(q,\omega)$ at small ω. This double-peak structure of $M_s(q,\omega)$, with peaks at $\omega \approx 0$ and $\omega \approx \epsilon$, is forwarded, for $q \to 0$, to the power spectrum of the VACF, $Z(\omega)$.

APPENDIX C: FITTING MODEL FOR THE COLLECTIVE DYNAMIC PROPERTIES

The initial values of $F(q,t)$ and its memory functions are also given through the frequency moments $\omega^{(0)}$, $\omega^{(2)}$, and $\omega^{(4)}$, whose expressions involve only the atomic positions, velocities, and accelerations,[12] and therefore they are readily obtained from the AIMD simulations. These values are imposed in the fitting of the first-order memory function $M(q,t)$.

In the GCM approach with n dynamic variables the intermediate scattering functions and other correlation functions are obtained as linear combinations of n exponential functions with either real or complex amplitudes and exponents (in the latter case in complex-conjugate pairs). The real terms correspond to relaxing (diffusionlike) modes while the complex-conjugate pairs correspond to propagating modes. The exponents of the functions are the eigenvalues of a generalized hydrodynamic matrix constructed from the variables used in the GCM approach and the corresponding eigenvectors specify explicitly the character of the eigenmodes. The number of variables used is to some extent arbitrary but usually the three conserved hydrodynamic variables (density, longitudinal current and energy density) are always considered. Additional variables can be added to these three, reflecting nonconserved variables that can be important outside the hydrodynamic region, as, for instance, time derivatives of the longitudinal current or of the energy density. Such a five-variable approach has been studied in detail by Bryk and collaborators,[56] both analytically for small q, and numerically in a wide q region for Lennard-Jones systems and liquid metals through MD simulations.

As mentioned in the main text, the most general GCM approach cannot be followed in *ab initio* simulations. However from a mathematical point of view we know that the results for $F(q,t)$ within a five-variable approach will be given by a sum of five exponentials. This immediately means that the first memory function $M(q,t)$ will be a sum of four exponential terms and the second memory function $N(q,t)$ a sum of three exponential functions. The values of the exponents and amplitudes in $F(q,t)$, $M(q,t)$, and $N(q,t)$, as well

as their being real or complex, can (and do) change as a function of q.

We have used this type of expression in order to fit the simulation results, in particular, at the level of $M(q,t)$. We found that for $q \leq 0.9$ Å^{-1}, two pairs of complex-conjugate terms are needed whereas for $0.9 \leq q \leq 1.05$ Å^{-1} a pair of complex-conjugate terms and two real terms are required. Now, for $1.05 \leq q \leq 1.80$ Å^{-1} one of the real exponentials becomes extremely fast decaying but with a very small amplitude. The net effect is that it is possible to incorporate it into the other three exponential terms while in $N(q,t)$ one of the three exponentials changes into a Dirac delta function. Within the range $1.80 \leq q \leq 2.5$ Å^{-1}, two pairs of complex-conjugate terms are again necessary to achieve a good fit; and, finally, up to $q \leq 3$ Å^{-1} the best fit is obtained with the same model as for $M_s(q,t)$, namely, that corresponding to a zero-frequency term and a high-frequency term.

As we have just stated, the form of the second-order memory function is given either as a sum of three exponential terms or as two exponentials and a Dirac delta function. In this second case, which applies when q is in the range $1.05 < q \leq 1.8$ Å^{-1}, the two exponentials are always real and, therefore, the model for $N(q,t)$ comprises a slowly decaying term, another that decays fast and finally an "instantaneously" decaying one,

$$N(q,t) = A_s \exp[-g_s t] + A_f \exp[-g_f t] + 2B_i \delta(t),$$

$$\tilde{N}(q,z) = \frac{A_s}{z+g_s} + \frac{A_f}{z+g_f} + B_i. \tag{C1}$$

In a small q range of the three exponential region for $N(q,t)$, namely, for $0.9 < q \leq 1.0$ Å^{-1}, the three terms are real, with components decaying slowly, fast, and very fast,

$$N(q,t) = A_s \exp[-g_s t] + A_f \exp[-g_f t] + A_v \exp[-g_v t],$$

$$\tilde{N}(q,z) = \frac{A_s}{z+g_s} + \frac{A_f}{z+g_f} + \frac{A_v}{z+g_v}. \tag{C2}$$

Finally, in the rest of the q range studied, two of the terms are complex conjugate of each other and one is real, leading to the expressions

$$N(q,t) = A_s \exp[-g_s t] + \exp[-g_f t][A_f \cos(\mu t) + B_f \sin(\mu t)],$$

$$\tilde{N}(q,z) = \frac{A_s}{z+g_s} + \frac{A_f(z+g_f) + B_f \mu}{\mu^2 + (z+g_f)^2}. \tag{C3}$$

Therefore, we have a slow and a fast (oscillating) term.

We stress that the model for $N(q,t)$ is always a three-exponential model; it is only the values of the coefficients that change with q.

The separation into a slow part and the rest (fast or fast plus very fast) is important in order to understand the physical origin of these terms. In particular, if the slow component is related to thermal relaxation, then its initial value will be connected to the generalized specific heat ratio $\gamma(q)$ through the relation

$$A_s(q) = M(q,0)[\gamma(q) - 1]. \tag{C4}$$

On the other hand, if the slow component is related to viscoelastic relaxation, then the relation with $\gamma(q)$ is

$$A_s(q) = N(q,0) - M(q,0)[\gamma(q) - 1]. \tag{C5}$$

These two possibilities, together with the expected variation in $\gamma(q)$ with q, and, in particular, its value for $q \to 0$, are used in the text in order to establish the physical origin of the different terms.

We indicate now the expressions obtained for $F(q,t)$ within the different q regions. In the two exponentials plus delta function region, $F(q,t)$ is given as a sum of four exponential terms, of which two are real and the other two are complex conjugate of each other,

$$F(q,t) = A_1 \exp[-D_1 t] + A_2 \exp[-D_2 t] + \exp[-\Gamma_1 t] \times \{B_1 \cos(\omega_1 t) + C_1 \sin(\omega_1 t)\}. \tag{C6}$$

In a small q region, between 0.9 and 1.05 Å^{-1}, an additional real exponential appears, so a term $A_3 \exp[-D_3 t]$ must be added to the previous expression. Finally, in the rest of the q region, which includes both the long-wavelength region and the first peak of $S(q)$, the intermediate scattering function comprises a real exponential and two pairs of complex-conjugate terms,

$$F(q,t) = A_1 \exp[-D_1 t] + \exp[-\Gamma_1 t]\{B_1 \cos(\omega_1 t) + C_1 \sin(\omega_1 t)\} + \exp[-\Gamma_2 t]\{B_2 \cos(\omega_2 t) + C_2 \sin(\omega_2 t)\}. \tag{C7}$$

Note that the contribution of an exponential term of $F(q,t)$ to the dynamic structure factor $S(q,\omega)$ has the Lorentzian form

$$\frac{1}{\pi} \frac{A_j D_j}{\omega^2 + D_j^2}, \tag{C8}$$

while a damped oscillatory term will contribute to $S(q,\omega)$ with the term

$$\frac{1}{\pi} \frac{(B_j \Gamma_j + C_j \omega_j)\omega_{c;j}^2 + (B_j \Gamma_j - C_j \omega_j)\omega^2}{(\omega^2 - \omega_{c;j}^2)^2 + 4\Gamma_j^2 \omega^2}, \tag{C9}$$

where $\omega_{c;j}^2 = \omega_j^2 + \Gamma_j^2$. Sometimes the term in the numerator proportional to ω^2 is neglected; for instance, in the model used by Sani *et al.*[11] to fit the inelastic line obtained from their experimental measurements (incidentally, their damping factor is equivalent to twice our Γ). However, as we indicate in the main text, this neglect leads to an "effective" damping factor smaller than the real one.

Finally, it should be noted that we define the "amplitude" of a damped propagating mode as the modulus of the complex number $(B_j + iC_j)$, i.e., as $\sqrt{B_j^2 + C_j^2}$, while the amplitude of a diffusivelike mode is defined as $|A_j|$.

[1] P. Hohenberg and W. Kohn, Phys. Rev. **136**, B864 (1964).
[2] W. Kohn and L. J. Sham, Phys. Rev. **140**, A1133 (1965).
[3] R. Bellissent, C. Bergman, R. Ceolin, and J. P. Gaspard, Phys. Rev. Lett. **59**, 661 (1987).
[4] Y. Greenberg, E. Yahel, E. N. Caspi, C. Benmore, B. Beuneu, M. P. Dariel, and G. Makov, EPL **86**, 36004 (2009).
[5] D. M. North, J. E. Enderby, and P. A. Egelstaff, J. Phys. C **1**, 1075 (1968).
[6] U. Dahlborg and M. Davidovič, Phys. Chem. Liq. **15**, 243 (1986).
[7] Y. Waseda, *The Structure of Non-Crystalline Materials* (McGraw-Hill, New York, 1980).
[8] U. Dahlborg and L. G. Olsson, Phys. Rev. A **25**, 2712 (1982).
[9] U. Dahlborg and L. G. Olsson, J. Phys. F: Met. Phys. **13**, 555 (1983).
[10] K. Shibata, S. Hoshino, and H. Fujishita, J. Phys. Soc. Jpn. **53**, 899 (1984).
[11] L. Sani, L. E. Bove, C. Petrillo, and F. Sacchetti, J. Non-Cryst. Solids **353**, 3139 (2007).
[12] U. Balucani and M. Zoppi, *Dynamics of the Liquid State* (Clarendon, Oxford, 1994).
[13] T. Scopigno, G. Ruocco, and F. Sette, Rev. Mod. Phys. **77**, 881 (2005).
[14] I. H. Umar and W. H. Young, J. Phys. F: Met. Phys. **4**, 525 (1974).
[15] P. Ascarelli, Phys. Rev. **173**, 271 (1968).
[16] M. Dzugutov and U. Dahlborg, Phys. Rev. A **40**, 4103 (1989).
[17] J. Hafner and W. Jank, Phys. Rev. B **45**, 2739 (1992).
[18] T. Bryk and I. Mryglod, J. Phys.: Condens. Matter **12**, 3543 (2000); **13**, 1343 (2001).
[19] G. A. de Wijs, G. Pastore, A. Selloni, and W. van der Lugt, Phys. Rev. Lett. **75**, 4480 (1995).
[20] G. A. de Wijs, Ph.D. thesis, Rijkuniversiteit Groningen, 1995.
[21] See http://www.ices.utexas.edu/parsec/
[22] T. L. Beck, Rev. Mod. Phys. **72**, 1041 (2000).
[23] M. M. G. Alemany, M. Jain, L. Kronik, and J. R. Chelikowsky, Phys. Rev. B **69**, 075101 (2004); M. M. G. Alemany, M. Jain, M. L. Tiago, Y. Zhou, Y. Saad, and J. R. Chelikowsky, Comput. Phys. Commun. **177**, 339 (2007).
[24] N. Troullier and J. L. Martins, Phys. Rev. B **43**, 1993 (1991).
[25] L. Kleinman and D. M. Bylander, Phys. Rev. Lett. **48**, 1425 (1982).
[26] D. M. Ceperley and B. J. Alder, Phys. Rev. Lett. **45**, 566 (1980).
[27] J. P. Perdew and A. Zunger, Phys. Rev. B **23**, 5048 (1981).
[28] N. Binggeli, J. L. Martins, and J. R. Chelikowsky, Phys. Rev. Lett. **68**, 2956 (1992).
[29] D. Beeman, J. Comput. Phys. **20**, 130 (1976).
[30] H. Hellmann, *Einführung in die Quantenchemie* (Deuticke, Leipzig, 1937); R. P. Feynman, Phys. Rev. **56**, 340 (1939).
[31] X. G. Gong, G. L. Chiarotti, M. Parrinello, and E. Tosatti, Europhys. Lett. **21**, 469 (1993).
[32] L. E. González, D. J. González, and M. J. Stott, Phys. Rev. B **77**, 014207 (2008).
[33] L. Calderín, D. J. González, L. E. González, and J. M. López, J. Chem. Phys. **129**, 194506 (2008).
[34] L. Gao, P. Li, H. Lu, S. F. Li, and Z. X. Guo, J. Chem. Phys. **128**, 194304 (2008).
[35] R. L. McGreevy, A. Baranyai, and I. Ruff, Phys. Chem. Liq. **16**, 47 (1986).
[36] S. Takeda, S. Tamaki, and Y. Waseda, J. Phys. Soc. Jpn. **54**, 2552 (1985).
[37] J. R. D. Copley and S. W. Lovesey, Rep. Prog. Phys. **38**, 461 (1975).
[38] T. Gaskell and S. Miller, J Phys. C **11**, 3749 (1978).
[39] J. P. Hansen and I. R. McDonald, *Theory of Simple Liquids* (Academic Press, New York, 1986); J. P. Boon and S. Yip, *Molecular Hydrodynamics* (McGraw-Hill, New York, 1980).
[40] A. Delisle, D. J. Gonzalez, and M. J. Stott, Phys. Rev. B **73**, 064202 (2006); J. Phys.: Condens. Matter **18**, 3591 (2006).
[41] G. Doge, Z. Naturforsch. A **20**, 634 (1965).
[42] K. B. Larsen, Ph.D. thesis, MIT, 1964.
[43] N. Petrescu and M. Petrescu, Rev. Roum. Chim. **15**, 189 (1970).
[44] J. D. Chai, D. Stroud, J. Hafner, and G. Kresse, Phys. Rev. B **67**, 104205 (2003).
[45] M. M. G. Alemany, R. C. Longo, L. J. Gallego, D. J. González, L. E. González, M. L. Tiago, and J. R. Chelikowsky, Phys. Rev. B **76**, 214203 (2007).
[46] L. Calderín, L. E. González, and D. J. González, J. Chem. Phys. **130**, 194505 (2009).
[47] D. J. González, L. E. González, J. M. López, and M. J. Stott, J. Chem. Phys. **115**, 2373 (2001); Phys. Rev. B **65**, 184201 (2002).
[48] A. Torcini, U. Balucani, P. H. K. de Jong, and P. Verkerk, Phys. Rev. E **51**, 3126 (1995).
[49] F. Shimojo, K. Hoshino, and M. Watabe, J. Phys. Soc. Jpn. **63**, 141 (1994).
[50] S. Kambayashi and G. Kahl, Phys. Rev. A **46**, 3255 (1992); G. Kahl and S. Kambayashi, J. Phys.: Condens. Matter **6**, 10897 (1994).
[51] J. Casas, D. J. González, and L. E. González, Phys. Rev. B **60**, 10094 (1999).
[52] J. Casas, D. J. González, L. E. González, M. M. G. Alemany, and L. J. Gallego, Phys. Rev. B **62**, 12095 (2000).
[53] M. M. G. Alemany, L. J. Gallego, and D. J. González, Phys. Rev. B **70**, 134206 (2004).
[54] S. Blairs, Phys. Chem. Liq. **45**, 399 (2007).
[55] I. M. de Schepper, E. G. D. Cohen, C. Bruin, J. C. van Rijs, W. Montfrooij, and L. A. de Graaf, Phys. Rev. A **38**, 271 (1988); I. M. Mryglod, I. P. Omelyan, and M. V. Tokarchuk, Mol. Phys. **84**, 235 (1995).
[56] T. Bryk and I. Mryglod, Condens. Matter Phys. **7**, 471 (2004).
[57] T. Bryk and I. Mryglod, Condens. Matter Phys. **11**, 139 (2008).
[58] M. Canales, L. E. González, and J. A. Padró, Phys. Rev. E **50**, 3656 (1994).
[59] T. Bryk and I. Mryglod, Phys. Rev. E **63**, 051202 (2001).
[60] J. Vollmann and D. Riedel, J. Phys.: Condens. Matter **8**, 6175 (1996).
[61] R. Kubo, J. Phys. Soc. Jpn. **12**, 570 (1957); D. A. Greenwood, Proc. Phys. Soc. London **71**, 585 (1958).
[62] F. Sar, S. Mhiaoui, and J.-G. Gasser, J. Non-Cryst. Solids **353**, 3622 (2007).